Doping in the Valley of Hydrogen Solubility: A Route to Designing Hydrogen-Resistant Zirconium Alloys

Mostafa Youssef, Ming Yang, and Bilge Yildiz

Phys. Rev. Applied **5**, 014008 — Published 26 January 2016

DOI: 10.1103/PhysRevApplied.5.014008

Doping in the Valley of Hydrogen Solubility: A Route to Design Hydrogen Resistant Zirconium Alloys

Mostafa Youssef[1], Ming Yang[1], Bilge Yildiz[1,2]*

[1]Laboratory for Electrochemical Interfaces, Department of Nuclear Science and Engineering, Massachusetts Institute of Technology, 77 Massachusetts Avenue, Cambridge, MA 02139, USA.

[2]Department of Materials Science and Engineering, Massachusetts Institute of Technology, 77 Massachusetts Avenue, Cambridge, MA 02139, USA.

*Correspondence to: byildiz@mit.edu

ABSTRACT

Hydrogen pickup and embrittlement pose a challenging safety limit for structural alloys used in a wide range of infrastructure applications, including zirconium alloys in nuclear reactors. Previous experimental observations guided the empirical design of new hydrogen resistant zirconium alloys, but the underlying mechanisms remained undecipherable. Here, we assess two critical prongs of hydrogen pickup through the ZrO_2 passive film that serves as a surface barrier of zirconium alloys; the solubility of hydrogen in it – a detrimental process, and the ease of H_2 gas evolution from its surface – a desirable process. By combining statistical thermodynamics and density functional theory calculations, we show that hydrogen solubility in ZrO_2 exhibits a valley-shape as a function of the chemical potential of electrons, μ_e. Here, μ_e , which is tunable by doping, serves as a new physical descriptor of hydrogen resistance based on the electronic structure of ZrO_2. For designing zirconium alloys resistant against hydrogen pickup, we target either a dopant that thermodynamically minimizes the solubility of hydrogen in ZrO_2 at the

bottom of this valley (such as Cr), or a dopant that maximizes μ_e and kinetically accelerates proton reduction and H_2 evolution at the surface of ZrO_2 (such as Nb, Ta, Mo, W, or P). Maximizing μ_e also promotes the predomination of a less mobile form of hydrogen defects, which can reduce the flux of hydrogen uptake. The analysis presented here for the case of ZrO_2 passive film on Zr alloys serves as a broadly-applicable and physically-informed framework to uncover doping strategies to mitigate hydrogen embrittlement also in other alloys, such as austenitic steels or nickel-alloys, which absorb hydrogen through their surface oxide films.

I. INTRODUCTION

The unwanted yet ineluctable interaction of hydrogen with metal oxides dictates the performance of these oxides in their applications by impacting their electronic [1-4] and mechanical properties [5,6]. Of focus to this paper is hydrogen pickup via zirconium oxide (ZrO_2) followed by embrittlement in zirconium alloys which are used as cladding for the fuel in nuclear reactors. Atomic hydrogen from a variety of sources reduces the ductility and toughness of metals [7]. When a water-containing environment induces oxidative corrosion of the metal, the resulting byproduct hydrogen may enter the metal from its surface. In the case of zirconium alloys, this process is regulated by a barrier oxide layer, that is ZrO_2 which grows natively on these alloys [8]. Hydrogen embrittlement of zirconium alloys poses a safety challenge to the operation of nuclear reactors because of the reduced ability of the metal to bear load before fracture. A fundamental understanding of the interaction of hydrogen with ZrO_2 is necessary to then allow for designing utmost reliable alloys that can suppress the source term for hydrogen entry into the underlying metal. In this work we explain how doping ZrO_2 can affect its capacity to absorb

hydrogen or to discharge hydrogen gas from its surface, and suggest design strategies that mitigate the ingress of hydrogen into the alloy through this barrier oxide.

Hydrogen pickup in zirconium alloys is usually expressed as the ratio between the hydrogen that enters the alloy and the total amount of hydrogen generated from the oxidation of zirconium by water. The ZrO_2 layer that grows natively on zirconium alloys regulates the entry of hydrogen to the underlying alloy [8,9]. Thus, it is anticipated that the impact of the alloying elements on hydrogen pickup takes place via the ZrO_2 layer. 3d transition metals that have been traditionally used for alloying zirconium have limited solubility in this metal, and they tend to precipitate as intermetallic compounds. Both the dissolved and precipitated components of the transition metals are oxidized progressively as they become part of the ZrO_2 layer [10] and so they provide a source for transition metal defects in the ZrO_2 lattice. Protons are produced upon the splitting of water at the ZrO_2/water interface [11]. This is followed by two competing scenarios. In the first, protons at the surface are incorporated into and diffuse through ZrO_2 in the form of various hydrogen defects and eventually reach the underlying alloy – this is the detrimental outcome. In the second scenario, electrons generated by the oxidation of the underlying alloy transport through ZrO_2 and transfer to the protons to reduce them at the surface, and eventually they evolve as H_2 molecules – this is the desired outcome to avoid hydrogen ingress into the metal. On the other hand, electron transport across ZrO_2 is thought to be the slowest process in zirconium corrosion [12], therefore it can decide the competition between hydrogen pickup and H_2 gas evolution.

In this study, we combine density functional theory (DFT) and thermodynamic analysis [13] to model the solubility of hydrogen in the oxide bulk and the ability to transfer electrons at the surface of monoclinic ZrO_2 (M-ZrO_2) as a function of dopant elements under oxygen rich

conditions (representative of the oxide/water interface). By incarnating the chemical potential of electrons, μ_e, as a physical descriptor for hydrogen solubility and electron availability in ZrO_2, we calculate a general hydrogen solubility curve as a function of μ_e for doped ZrO_2. The resulting curve has a valley shape. In the limit of non-interacting defects, we can map onto this solubility curve any compositions of doped ZrO_2. The valley of hydrogen solubility in ZrO_2 provides design strategies for zirconium alloys either based on the minimum hydrogen solubility in M-ZrO_2 (by Cr doping) or based on the maximum achievable kinetics of proton reduction at the surface of M-ZrO_2 (by Nb, Ta, Mo, W, or P doping). As another utility of this solubility curve, we showed that hydrogen solubility in doped ZrO_2 exhibits a volcano-like dependence across the 3d transition metals as dopants, in a strong similarity with the experimentally determined [14] hydrogen pickup fraction in zirconium alloys as a function of these elements. The results herein provide the first physically-grounded framework to study hydrogen pickup in zirconium alloys, with special attention to the passive layer's ability to dissolve hydrogen and to reduce protons.

The framework and the physical descriptor presented here to analyze the impact of doping on the resistance of the surface oxide layer against hydrogen penetration into the underlying metal have broader applicability than the ZrO_2/Zr-alloy system. All refractory metallic alloys develop a protective corrosion layer at their surface, such as Cr-, Fe- and Ni-oxide layers on steels and Ni-based alloys. There is evidence that these surface oxide layers affect the penetration of hydrogen into the underlying metal [15], and as such we propose that they can be engineered by doping to resist hydrogen entry. By computing the formation free energies of all hydrogen defects in these oxides, it is possible to determine general hydrogen solubility curves as a function of μ_e in these oxides. Here we show that this general solubility

curve has a valley-shape in ZrO_2 thanks to having both a positive and a negative predominant hydrogen defects as we detail below. But in other surface oxides, this curve could have a different shape – be monotonically increasing, monotonically decreasing or exhibiting a plateau – depending on the charge states of the predominant hydrogen defects. Based on the shape of the hydrogen solubility curve, it is possible to propose doping schemes that minimizes hydrogen entry either by reducing the solubility of hydrogen or by accelerating the proton reduction and H_2 evolution at the surface of the oxide. It is, thus, possible to adopt the herein presented framework to design corrosion layers that help in mitigating hydrogen embrittlement of metallic alloys. Contrary to the empirical doping schemes typically adopted by the industry, including the nuclear fuel industry, our framework is informed by first-principles evaluation of defect formation free energies and employs key concepts from semiconductors physics (electron chemical potential) and catalysis (electron transfer and redox reactions) to pinpoint effective doping strategy to resist hydrogen embrittlement.

The organization of the rest of the paper is as follows. In section II we present the methodology adopted in this work, in section III the results and discussion, and concluding remarks are included in section IV.

II. METHODS

A. Structure and Charge State of Defects

In this study we considered the native defects, hydrogen defects and an alloying element (3d transition metals, Sn, Nb, Ta, W, Mo or P) defects in monoclinic ZrO_2 (M-ZrO_2). The native defects we examined are the vacancies and interstitials of both oxygen and zirconium. The initial guess for the interstitial site was the geometric center of the unit cell of M-ZrO_2 and no systematic search for the lowest energy interstitial site was conducted. The asymmetric crystal

structure of M-ZrO_2 aided the relaxation to a reasonably low energy configuration of the interstitial defect starting from our initial guess. Defects due to mono-hydrogen and di-hydrogen in interstitial site, substituting oxygen, and substituting zirconium were studied. Similar to the native interstitial defects, the initial guess for the interstitial hydrogen defect is the geometric center of the unit cell of M-ZrO_2. For all di-hydrogen defects, the initial guess was such that the two hydrogen species are separated by the H_2 molecule bond length and oriented in the <001> direction. We examined the clustering of 3 and 4 hydrogen species in zirconium vacancies [16], but we found out that hydrogen does not have a clustering tendency in the cations vacancies of the monoclinic ZrO_2. Alloying elements defects considered here are expected to be present as substitutional defects on the cation sublattice. In addition to this expected site, we also examined interstitial sites (except for Mo,) and in the case of P we also considered substitution on the anion sublattice. As before the initial guess for the interstitial metal defects is the geometric center of the unit cell of M-ZrO_2.

For each defect we considered multiple charge states. The minimum and maximum charge states for each elementary defect (one that is not a complex) are summarized in the Supplemental Material, section 1 [17]. Substitutional defects are considered as defect complexes due to association between an interstitial impurity and a native vacancy. The minimum and maximum charge states examined for each defect complex are the sum of the minima and maxima, respectively, of the charge states of the elementary defects that constitute this complex. By analyzing Bader charges and spins [18,19] of the ions surrounding the defect and examining the DFT calculated charge density, we were able to conclude the charge states that can be stabilized on or around the defect site without electron or hole delocalization [20]. Given the large number of defects considered in this study, we limited the charge localization analysis to

the defects that has a concentration greater than 10^{-16} at 600K in a range of oxygen partial pressure between 1 atm and 10^{-15} atm. The outcome of this analysis is provided in the Supplemental Material, section 2 [17].

B. Construction of Kröger-Vink Diagrams

We construct the Kröger-Vink diagram for monoclinic ZrO_2 co-doped with hydrogen and a transition metal by applying the charge neutrality condition to the concentrations of electronic and ionic defects. The details of the approach were described in our recent work [13,21] and here we outline the notions relevant to the current study.

The concentrations of the conduction band electrons and valence band holes were obtained by applying Fermi-Dirac statistics to the DFT calculated electronic density of states of undoped M-ZrO_2. On the other hand the concentrations of ionic defects were calculated by minimizing the free energy of the defect-containing crystal under the assumption of non-interacting defects. This minimization requires the free energy of formation of the ionic defects as an input. By neglecting the stress-volume term which is compatible with the limit of non-interacting defects, the free energy of formation of a defect *d* with charge *q* is defined as

$$G^f_{d,q} = (E^{def}_{pot} + F^{def}_{vib}) - (E^{perf}_{pot} + F^{perf}_{vib}) + \sum_k \Delta n_k \mu_k + q(E_{VBM} + \mu_e) + E_{corr}, \quad (1)$$

where E^{def}_{pot} and E^{perf}_{pot} are the energies of the defective and perfect crystals, respectively. Similarly, F^{def}_{vib} and F^{perf}_{vib} are the vibrational free energies of the defective and perfect crystal, respectively. Δn_k is the difference between the number of ions of the species *k* in the perfect crystal and the number of ions of the same species in the defective crystal, μ_k is the chemical potential of the species *k*, E_{VBM} is the energy of the valence band maximum in the perfect crystal,

and μ_e is the chemical potential of electrons which is also known as the Fermi level. The zero of μ_e is chosen to be coincident with E_{VBM} and hence μ_e ranges from zero up to the value of the band gap of the perfect crystal as calculated using DFT. For M-ZrO_2, the DFT calculated band gap is 3.5 eV, which is underestimated compared to the experimental values of 4.2 eV determined using electron energy-loss spectroscopy [22] or 5.8 eV determined using ultraviolet spectroscopy [23]. In this work, if the equilibrium value for μ_e is greater than $E_{VBM} + \frac{1}{2}E_{gap}$ we describe M-ZrO_2 as n-type doped, whereas if μ_e is less than $E_{VBM} + \frac{1}{2}E_{gap}$, M-$ZrO_2$ is considered to be p-type doped. Finally E_{corr} is a correction to account for simulating charged defects in a finite supercell. In this work we adopted the first order Makov-Payne (MP1) correction [24]. In applying this correction we used a scalar static dielectric constant of 20 as an average for the dielectric tensor which we calculated using density functional perturbation theory [25] to be ($\varepsilon_{11} = 24$, $\varepsilon_{22} = 22$, $\varepsilon_{33} = 18$, $\varepsilon_{13} = 1$). Our calculations of the dielectric tensor are in line with prior theoretical work [26,27]. Inspecting the tensor shows that the off-diagonal terms are very small and that the diagonal terms almost isotropic. This justifies using a scalar dielectric constant in applying the Makov-Payne correction. Moreover, it was shown for the fully ionized anion and cation vacancy in the isostructural and chemically similar monoclinic HfO_2 that the anisotropy in the dielectric tensor have a negligible effect on the value of the charged supercell correction [28]. In section 3 of the Supplemental Material [17] we compare the performance of the MP1 correction to the computationally expensive finite size scaling correction [29] for selected defects. With respect to finite size scaling correction, the maximum error for the MP1 corrected formation energies was found to be -0.51 eV in the case of $V_{Zr}^{""}$. On the other hand, the uncorrected results have a maximum error of -2.06 eV with respect to finite size scaling. In

general the MP1 correction was found to improve the uncorrected formation energies. While not perfect, the MP1 correction is suitable for this study which considers a large number of defects and it also reduces the error in electrostatics to within the range of other uncertainties such as the approximate DFT exchange correlation and the harmonic approximation for phonons.

It remains to clarify the values of the chemical potential of species μ_k used in equation (1). For the native defects, all what is needed is the chemical potential of oxygen μ_O from which the chemical potential of zirconium μ_{Zr} can be deduced [13,16]. For every Kröger-Vink diagram, μ_O was allowed to vary in a range that corresponds to a range of oxygen partial pressure, P_{O_2}, from 1 atm to10^{-15} atm. The defect equilibrium at P_{O_2} = 1 atm is considered to be representative of the oxygen rich part of ZrO_2, that is the surface of ZrO_2 interfacing with water in the nuclear reactor (see also section 12 and 14 in the Supplemental Material [17]). μ_O was obtained form P_{O_2} as

$$\mu_O(T,P_{O_2}) = \frac{1}{2}[E_{O_2}^{DFT} + E_{over} + \mu_{O_2}^0(T,P^0) + k_B T \ln\left(\frac{P_{O_2}}{P^0}\right)], \quad (2)$$

where $E_{O_2}^{DFT}$ is the calculated DFT energy of the oxygen molecule and E_{over} is a correction for the O_2 overbinding error caused by DFT. The details of obtaining this correction following the scheme proposed by Wang et al. [30] are described in the Supplementary Material, section 4 [17]. $\mu_{O_2}^0(T,P^0)$ is a reference chemical potential for O_2 gas at a reference pressure P^0 which is typically 1 atm. $\mu_{O_2}^0(T,P^0)$ was obtained from tabulated thermochemical data [31]. Hydrogen defects require a value for the chemical potential of hydrogen μ_H which in this work was computed as computed as

$$\mu_H(T) = \frac{1}{2}[\mu_{H_2O}(T, P_{H_2O} = 1atm) - \mu_O(T, P_{O_2} = 1atm)], \quad (3)$$

where μ_{H_2O} is calculated from P_{H_2O} using an equation similar to equation (2) except for the overbinding error which does not apply to the H_2O molecule. The choice of a μ_H dependent only on temperature in (3) represents the situation where water is only located at the oxygen rich part of the oxide (water/M-ZrO_2 interface) and provides the source term for all hydrogen defects throughout the oxide layer. Finally, the chemical potential of a transition metal μ_M was computed as

$$\mu_M(T, P_{O_2}) = \frac{y}{x}[\frac{1}{y}\mu_{M_xO_y} - \mu_O(T, P_{O_2})], \quad (4)$$

where $\mu_{M_xO_y}$ is the chemical potential of the metal oxide M_xO_y which is taken to be the DFT calculated energy for the chemical formula of this oxide. The choice of both T and P_{O_2} dependent chemical potential for the transition metal is consistent with the situation taking place in the zirconium alloy in the nuclear reactor. In this alloy the transition metal exists initially both dissolved in the alloy and as a intermetallic precipitates. Upon oxidation, these two components serve as the source term for the transition metal defects in zirconia. Since these alloying metals are distributed throughout the zirconium alloy, it is expected to be present throughout the zirconia layer and hence exposed to the gradient of the chemical potential of oxygen across the zirconia film as it grows. This justifies the aforementioned choice for P_{O_2} and T dependence of μ_M. More details about the reference oxides, M_xO_y, and discussion about the uncertainties in choosing the suitable reference are given in the Supplemental Material section 5 [17].

At a given equilibrium thermodynamic state, herein defined by T and P_{O_2}, we seek a unique and physically meaningful value of μ_e that forces the concentrations of ionic and

electronic defects to achieve charge neutrality [13]. By physically meaningful, we mean a value of μ_e which does not give rise to a negative formation energy of any defect and which is bounded by the edges of the valence band and conduction band [32]. By determining this unique μ_e value at every state, the Kröger-Vink diagram can be constructed. In this study we constructed the Kröger-Vink diagrams of M-ZrO_2 co-doped with hydrogen and a transition metal at 600 K which is a typical nuclear reactor operation temperature, whereas P_{O_2} was varied between 1 and 10^{-15} atm. We validated our predictions for the undoped oxide against the experimental findings as discussed in section A of the results and discussion. The calculated formation energies for all defects and the Kröger-Vink diagrams for co-doped M-ZrO_2 are provided in section 6 of the Supplemental Material [17].

Nb and Ta have high solubility in ZrO_2 and the approach of non-interacting defects is inadequate to describe them at their equilibrium solubility levels in ZrO_2. The negative formation energies found here for some of their defects in ZrO_2 is a direct evidence for such a high solubility for these elements. In this work, we overcome this issue by solving the charge neutrality condition while constraining the solution at a fixed doping level for Nb and Ta. That is to say we forced the sum of the concentrations of their defects in ZrO_2 to yield a priori fixed doping level. In doing so, we made sure that this fixed doping level corresponds to a dopant chemical potential less than that which leads to the solubility limit of these elements in ZrO_2. Furthermore, we made sure that this fixed doping level corresponds to positive formation energies for all the defects. Contrary to Nb and Ta, the elements Mo, W, and P have very low solubility in ZrO_2. In their respective cases, we also solved the charge neutrality condition by assigning a fixed doping level which is much higher than their solubility limit. In doing this, we acknowledge that the results do not represent an equilibrium solution. Instead, it is more

representative of a non-equilibrium situation in which these elements were forced to dissolve in ZrO_2. Such non-equilibrium situation could be enabled by dissolution under irradiation, or by other metastable materials processing routes [33].

C. Density Functional Theory Calculations.

We performed density functional theory calculations using the projector-augmented plane-wave method [34] as implemented in the code Vienna Ab initio simulation package (VASP) [35-38]. For every element in this study, a number of electrons are treated as core and hence frozen while the rest are treated as valence electrons. In section 7 of the Supplemental Material [17] we provide a list of the number of valence electrons for each element. The exchange-correlation was treated using the standard Perdew, Burke, and Ernzerhof (PBE) functional [39,40]. Although there is a tendency to prefer hybrid functionals that incorporate a fraction of the exact exchange in studying materials with electronic band gap, we found out that adopting standard PBE is a reasonable and optimal choice for the current study for three reasons. First, PBE is generally criticized for underestimating band gaps and a typical remedy for this would be employing an empirical on-site Coulomb interaction (the so-called DFT+*U* approach) to reproduce the experimental band gap. However, it turns out that hybrid functionals suffer a similar issue where one needs to tune the mixing and screening parameters to attain a desired band gap. For example, we used the screened hybrid functional of Heyd, Scuseria, and Ernzerhof (HSE) [41,42] with the standard 25% mixing of the exact screened exchange and a screening parameter of 0.2 $Å^{-1}$ and obtained a single particle Kohn-Sham band gap of 4.51 eV for M-ZrO_2 and a difference between the ionization potential (I) and electron affinity (A) of I – A = 5.18 eV for the same oxide. Ramprasad et al. [43] showed that by tuning the mixing and screening parameters of the HSE functional, the band gap of M-ZrO_2 can be varied between 4.5 eV and 6.5

eV. Given the wide scatter in the experimentally determined band gaps of M-ZrO_2 (4.2-5.8 eV) [22,23], we believe that empiricism is uncalled for here and resorting to standard functionals is reasonable. In section 8 of the Supplemental Material [17] we attempt applying a rigid shift of the conduction band on top of the PBE band gap and show that this leads to inaccurate defect equilibria for undoped M-ZrO_2. Second, PBE is criticized for favoring delocalized electrons (or holes) due to the convexity of the PBE energy as a function of the continuous fractional occupation number whereas the correct dependence is straight line [44,45]. For M-ZrO_2 treated using PBE and for the purpose of this study, we found out that this issue is not severe as we discuss in the Supplemental Material, section 9 [17]. It should be noted that a hybrid functional can also suffer from this localization/delocalization problem especially if it was tuned to predict a certain band gap. Indeed using standard HSE with the mixing and screening parameters indicated above, we obtained a single particle Kohn-Sham gap that is different than I – A (4.51 eV vs. 5.18 eV). This fact already hints that this functional does not predict correct the straight line behavior of the energy as a function of the fractional occupation number [45]. Third, in this work we studied about 220 charge states for native, hydrogen, and alloying element defects and incorporated the contribution of phonons to the formation free energies for about 55 of them. Achieving such a task using a hybrid functional is formidable, hence it was overall logical to choose PBE for this study.

All defects calculations were performed in a supercell made of $2\times2\times2$ conventional unit cells of monoclinic ZrO_2. The lattice parameters and ionic positions in the relaxed unit cell of M-ZrO_2 are provided in section 10 of the Supplemental Material [17]. A kinetic energy cutoff of 450 eV and a $2\times2\times2$ Monkhorst-Pack k-point mesh were used throughout the computations. Spin-polarized energy minimization without any symmetry constraints was performed up to a

stopping criterion of 1 meV/Å. Such a strict criterion was needed to avoid imaginary frequencies during the subsequent vibrational free energy calculations. To accelerate the convergence of the electronic structure, we applied a Gaussian smearing with a smearing width of 0.05 eV.

To evaluate the vibrational free energy, we computed the vibrational frequencies of the relaxed defect super cells in the harmonic approximation. In these calculations a central finite-difference with a distance of 0.008 Å was used to construct the Hessian matrix. Since these computations are very expensive, we performed them only for the defects with concentrations greater than 10^{-16} at 600K in a range of oxygen partial pressure between 1atm and 10^{-15} atm. For the rest of the defects we assigned a typical value for the vibrational free energy, but such assigned value has no effect at all at the results conveyed here since the formation energies of these defects are very high. Only the gamma point was used during the DFT calculations of the vibrational frequencies. Then the code PHONOPY [46] was used to compute the phonon density of stated (DOS) using $15\times 15\times 15$ k-point mesh centered at the gamma point and subsequently the harmonic vibrational free energy was computed.

In order to calculate the concentration of free electrons and holes, the electronic DOS was computed for the perfect crystal of M-ZrO_2 using a 96 ions supercell. For this calculation we employed a dense $6\times 6\times 6$ k-point mesh centered at the gamma point in combination with the tetrahedron method with Blöchl corrections [47] .

III. RESULTS AND DISCUSSION

A. Native defects of monoclinic ZrO_2.

To enable a reference point of hydrogen solubility before assessing the effects of transition metal dopants, we computed the defect equilibria in the undoped M-ZrO_2. For this material, we present in Figure 1a the calculated Kröger-Vink diagram at 1200 K. Evaluation of

the defect equilibria at such a high temperature was performed to enable comparison with experiments. The diagram shows that M-ZrO_2 exhibits both p-type and n-type conductivity. The p-type behavior is found at high oxygen pressures, P_{O_2}, where holes, p_v, are compensated by doubly charged oxygen interstitials, $O_i^{''}$. At this temperature, the transition from p-type to in n-type regime occurs at 10^{-10} atm. At lower P_{O_2} free electrons, n_c, predominate and the charge compensation is accommodated by doubly charged oxygen vacancies, $V_O^{\bullet\bullet}$, except at very low P_{O_2} where charge compensation is achieved by singly charged oxygen vacancies, $V_O^{\bullet}$.

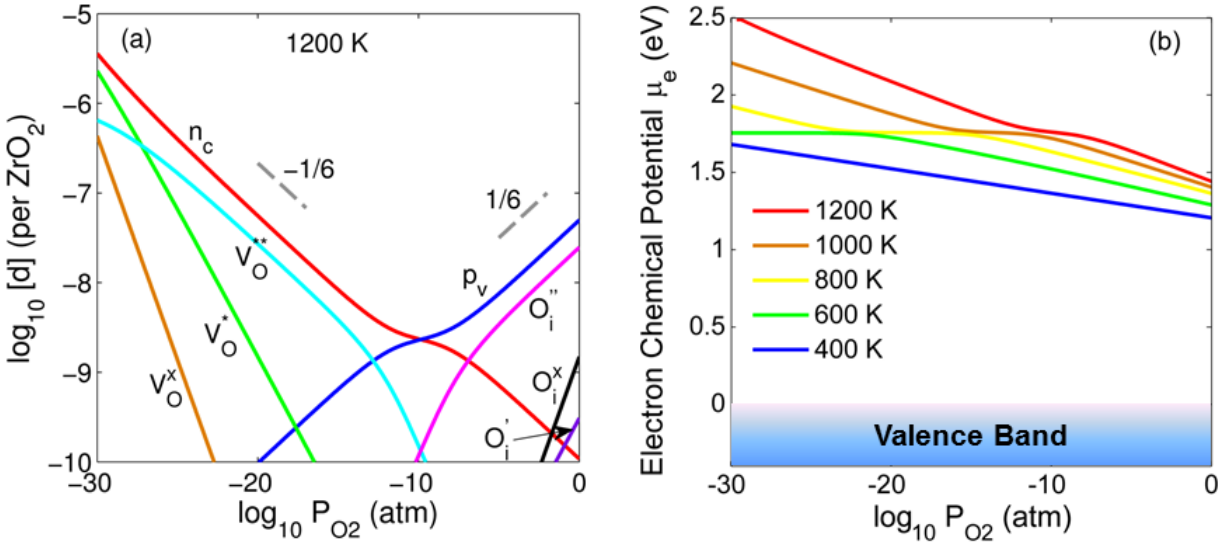

Figure 1. (a) Calculated Kröger-Vink diagram for the undoped monoclinic ZrO_2 at 1200 K. Point defects are represented by the Kröger-Vink notation, and n_c denotes conduction band electrons, and p_v denotes valence band holes. Only defects with concentrations, [d], greater than 10^{-10} per ZrO_2 are shown. The dashed lines are guide for the eye showing the slopes of (1/6) and (-1/6). (b) Calculated chemical potential of electrons that achieves charge neutrality in undoped monoclinic ZrO_2 as a function of T and P_{O_2}.

Both the measured electrical conductivity [48,49] and oxide off-stoichiometry [50] of M-ZrO_2 exhibit a slope of -1/6 with $\log_{10} P_{O_2}$ at low values of P_{O_2} and at temperatures as high as 1200 K. The forgone conclusion based on these experiments is that the -1/6 slope at low P_{O_2} is

due to the equilibrium established between free electrons and $V_O^{\bullet\bullet}$. Our theoretical predictions are in accordance with this conclusion. On the other hand, there is no experimental consensus on the slope that conductivity or off-stoichiometry exhibited with $\log_{10} P_{O_2}$ at high values of P_{O_2} .The experiments of reference [48] and [50] showed a slope of 1/5 which was interpreted as an equilibrium between holes and $V_{Zr}^{''''}$. On the other hand a slope of 1/4 was found in the electrical conductivity measurements of reference [49] and this was attributed to the compensation between holes and singly charged interstitial oxygen $O_i^{'}$. The discrepancy in the experimental findings could be, in part, due to the differences among the impurities within the samples. The role of these impurities becomes more pronounced at high P_{O_2} since the intrinsic defect concentrations are lower in that range. Our calculations revealed another complicating factor in the high P_{O_2} region. At high temperatures the predominant defects in the high P_{O_2} region are free holes and $O_i^{''}$ as in Figure 1a. However, at temperatures lower than 800 K the free holes are compensated by $V_{Zr}^{''''}$ as shown in Figure 2b below which is evaluated at 600 K. This change in the charge compensation mechanism can obstruct the accurate determination of the slope of either conductivity or off-stoichiometry at high P_{O_2}. According to our model and DFT formation free energies, this transition in charge compensation is the net outcome of three competing factors. By isobaric heating above 800K, the chemical potential of electrons μ_e increases as shown in Figure 1b, oxygen chemical potential decreases, and the change in vibrational free energy favors forming oxygen interstitials (See Figure S4 and Figure S4 in the Supplemental Material). The second and third factors win and they favor forming $O_i^{''}$. However, it is important to note that this quantitative description of the change in the charge compensation mechanism

depends on the accuracy of DFT-calculated formation free energies as discussed in the Methods and the sections 4 and 9 of the Supplemental Material.

Figure 1b shows the calculated μ_e that achieves charge neutrality in dopant-free M-ZrO_2 as a function of T and P_{O_2}. For all the temperatures depicted in the figure and at 1 atm, M-ZrO_2 is clearly in the p-type region (middle of the DFT-predicted band gap is at 1.75eV). Decreasing P_{O_2} isothermally leads to a gradual n-type self-doping via the native oxygen vacancies of the oxide. As indicated in the Methods section, we focus in this study on the value of μ_e at P_{O_2} = 1atm and 600K which are the representative conditions for the oxygen rich part of ZrO_2 in an operative nuclear reactor.

B. Defect equilibria in Hydrogen-doped monoclinic ZrO_2.

Impact of hydrogen on the defect equilibria of otherwise undoped M-ZrO_2 at 600 K is shown by the calculated Kröger-Vink diagram in **Figure 2**b. Hydrogen itself is regarded as a dopant in this framework. For comparison, the equilibria of the native defects in pure M-ZrO_2 at 600 K are shown in **Figure 2**a. Out of the large number of hydrogen defects we considered (See the Methods section), only three of them are of significant concentration in high (1 atm) to mid (~10^{-15} atm) oxygen partial pressure, P_{O_2}. These are a complex between a single hydrogen species and a zirconium vacancy in the charge state of 3-, $H_{Zr}^{'''}$, an interstitial proton, $H_i^{\bullet}$, and a complex between two hydrogen species and a zirconium vacancy in the charge state of 2-, $(2H)_{Zr}^{''}$. Without any other dopants in M-ZrO_2, $H_{Zr}^{'''}$ is the main compensator for electronic holes denoted by p_v in Figure 2. As we show below there is a rivalry between $H_{Zr}^{'''}$ and $H_i^{\bullet}$

which is settled by the value of μ_e that depends on the dopant in the oxygen-rich part of the oxide which is represented here at $P_{O_2} = 1$ atm.

In **Figure 2**c and d, we depict the relaxed atomic configurations of $H_{Zr}^{'''}$ and $H_i^{\bullet}$, respectively. In both defects, hydrogen is present as a proton attached to a threefold coordinated oxygen ion forming a hydroxyl group. However, we refer to $H_i^{\bullet}$ defect as an interstitial proton rather than a hydroxide ion following the convention adopted for this defect in semiconducting oxides [1]. This naming convention is justified especially because the proton in this defect tends to hop independently from one site to another by breaking an old hydroxyl group and forming a new one. Using the definition of reference [16], the calculated binding energy of the complex $H_{Zr}^{'''}$ is -2.0 eV indicating a strong thermodynamic stability. This implies a strong trapping and hindrance of mobility for the proton in this defect complex. More discussion about the hydrogen defects is given the Supplemental Material, section 11 [17].

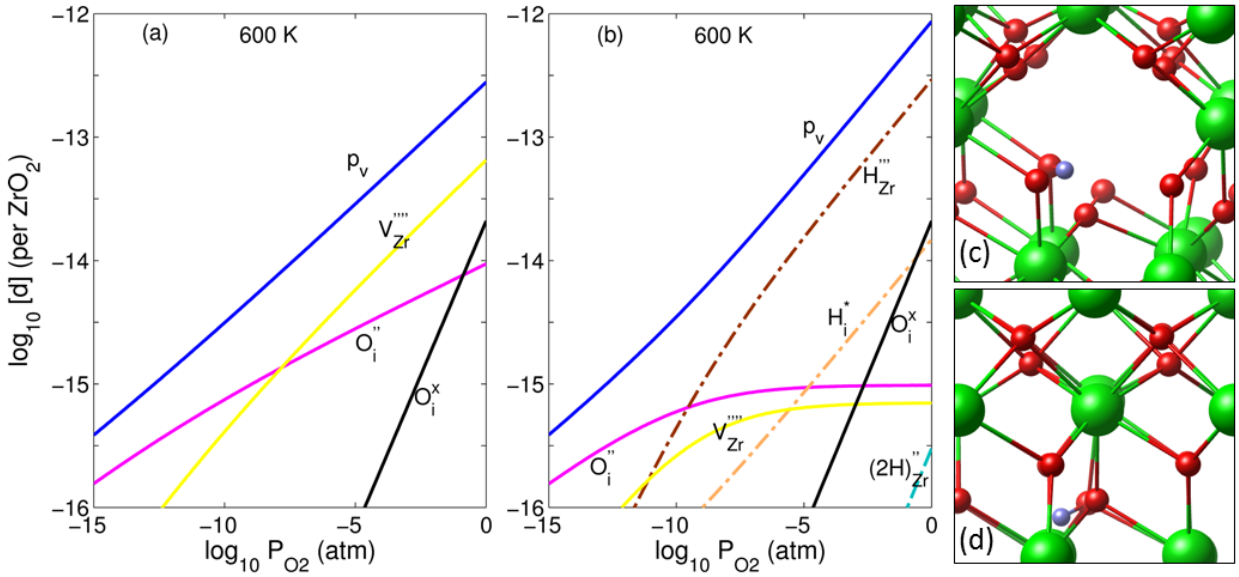

Figure 2. Calculated Kröger-Vink diagram for undoped (a) and hydrogen doped (b) monoclinic ZrO_2. Only the defects with concentration, [d], greater than 10^{-16} per ZrO_2 are shown. Point defects are denoted by the Kröger-Vink notation and p_v denotes the valence band holes. Hydrogen defects are shown by dashed-dotted lines. In (b) the results are evaluated at $P_{H_2O} = 1$

atm and using equation 3 for the chemical potential of hydrogen. (c) The relaxed structure of the complex formed between a hydrogen and a zirconium vacancy in the 3- charge state, $H_{Zr}^{'''}$. (d) The relaxed structure of the interstitial proton, $H_i^{\bullet}$. In panels (c) and (d), green (large), red (medium), and blue (small) balls represent zirconium, oxygen, and hydrogen, respectively. The visualizations in (c) and (d) were generated using the software VESTA[51].

C. Generalized hydrogen solubility in ZrO_2 – the *valley*

For design purposes, it is convenient to plot the hydrogen solubility as a function of a physical descriptor. Here, we provide a generalized dependence of hydrogen solubility on μ_e, which we designate as the physical descriptor in M-ZrO_2. This is done in the dilute limit without considering defect complexes of hydrogen and the other dopants in the oxide. The hydrogen solubility is calculated as the sum of the concentrations of all hydrogen defects which are, in turn, obtained from the free energy of formation of these defects at a given temperature and P_{O_2}. The resulting curves as a function of μ_e have a *valley shape*, shown in **Figure 3**a at three temperatures and under oxygen rich conditions representative of the water/oxide interface. The calculated valley shape is valid over a wide range of oxygen partial pressures (Supplemental Material, section 12 [17]). The implication of this curve for design is that by tuning the dopant choice and composition, one can tune μ_e in M-ZrO_2. Consequently, the impact of μ_e is two-fold; on the solubility of hydrogen in the bulk of M-ZrO_2, and on the rate of reduction of protons at the surface of M-ZrO_2. These design implications will be discussed specifically later.

The valley shape in **Figure 3**a can be expected naturally based on the formation free energy plot of the two predominant hydrogen defects, H_i and H_{Zr}, in **Figure 3**c. At μ_e smaller than that at the minimum of the solubility (that is the left arm of each solubility curve), $H_i^{\bullet}$ is the dominant defect, whereas at μ_e greater than that at the minimum of solubility (that is the

right arm) $H_{Zr}^{'''}$ is the dominant hydrogen defect in M-ZrO_2. The μ_e at the minimum of each solubility curve in **Figure 3**a is coincident with the μ_e at the intersection of the formation free energy lines of these two hydrogen defects as shown in **Figure 3**c. As temperature increases, the locus of the minimum shifts to higher values of μ_e because vibrational contribution to the formation free energies favors $H_i^{\bullet}$ compared to $H_{Zr}^{'''}$ (see Supplemental Material Figure S6 [17]).

The calculated solubility curves in **Figure 3** do not span the entire DFT-calculated band gap of M-ZrO_2 (3.5 eV), instead they are limited to a range in which the formation energies of all native and hydrogen defects are non-negative. For example, up to 900 K only the p-type region (i.e. $\mu_e < E_{VBM} + \frac{1}{2} E_{gap}$) is accessible by doping, indicating the difficulty of n-type doping in M-ZrO_2 at these thermodynamic conditions representative of the outer part of the oxide layer near the interface with water.

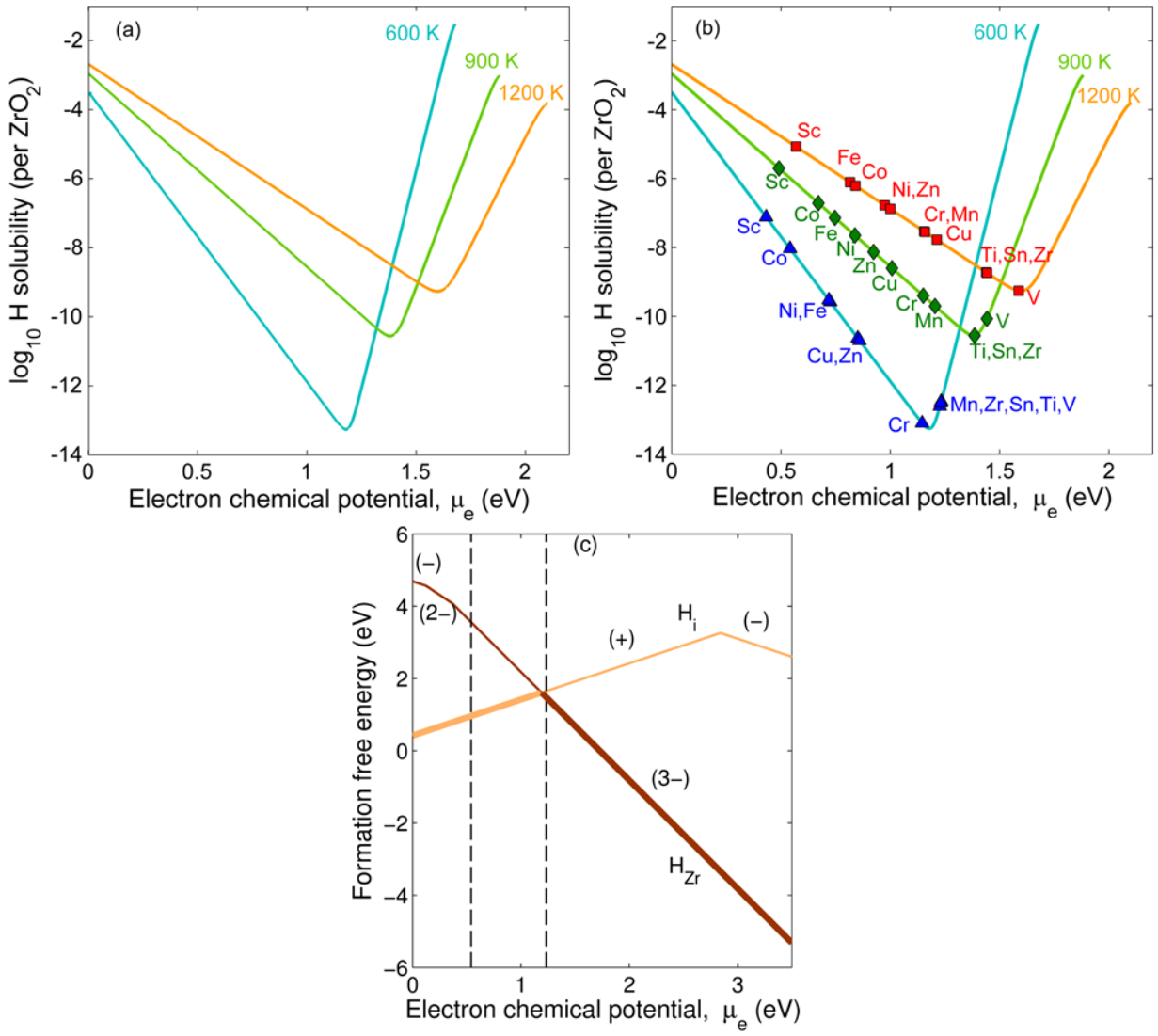

Figure 3. (a) The calculated solubility of hydrogen in monoclinic ZrO_2 as a function of the electron chemical potential (μ_e) at 600 K, 900 K and 1200 K. (b) On each solubility curve, we map 11 elements for which we explicitly calculated the value of μ_e that they establish at their solubility limit in monoclinic ZrO_2 when they co-dope it with hydrogen. The case of ZrO_2 doped with hydrogen but without any other elements is marked with 'Zr' as a reference point. The calculations in (a) and (b) were performed assuming P_{O_2} = 1 atm, and P_{H_2O} = 1 atm which are representative of the oxygen rich part of ZrO_2 in contact with water. The valley shape of the solubility curve is retained even at lower P_{O_2} conditions as we show in the Supplemental Material, section 12 [17]. (c) The formation free energy at 600 K of interstitial hydrogen, H_i, and the complex formed between hydrogen and a zirconium vacancy, H_{Zr}, as a function of μ_e. Only the charge states of these two defects with the lowest formation free energy are shown. The thick line traces the lowest formation free energy over all hydrogen defects as a function of μ_e.

The two vertical dashed lines correspond to the range of μ_e accessible by co-doping with hydrogen and a 3d transition metal, as spanned in Figure 4c from 0.54 eV to 1.23 eV.

Having established the general dependence of hydrogen solubility in M-ZrO_2 on μ_e in **Figure 3**a, we map 11 dopants onto each isothermal solubility curve in **Figure 3**b. The loci of these dopants on the solubility curves were calculated by solving the charge neutrality condition for the equilibrium μ_e that these elements establish when they dissolve up to *their solubility* limit in M-ZrO_2 and co-dope it together with hydrogen. These 11 dopants are 3d transition metals and Sn, and their solubilities in M-ZrO_2 range between 10^{-3} to 10^{-14} per ZrO_2 unit formula (see the Methods section). A subset of these 11 elements were used to develop the Zircaloy family of zirconium alloys [12]. For reference, when M-ZrO_2 is doped only with hydrogen, without any other metal dopant, we denote this on the curves by 'Zr'. At 600 K, Cr is the dopant closest to the minimum of the hydrogen solubility in M-ZrO_2. However, as the temperature increases, the distribution of the elements on the solubility valley changes due to the changes in defect equilibria. For example, at 1200 K, V minimizes the solubility of hydrogen in M-ZrO_2. Next, we employ our predictions of hydrogen solubility in doped M-ZrO_2 to provide an explanation for an intriguing empirical observation related to hydrogen pickup in zirconium alloys.

D. Hydrogen pickup in Zr – the *volcano*

A volcano-like dependence of hydrogen pickup in zirconium across the 3d transition metals that are used as alloying elements was identified in 1960 [14], as shown in **Figure 4**a. However, this empirically observed volcano behavior remained unexplained, and thereby going beyond this curve to design alloys that minimize hydrogen pickup on physical understanding has

been impossible. Being the gate to the underlying metallic alloy, it is reasonable to anticipate that the capacity of the oxide layer to absorb hydrogen should exhibit a similar dependence on the 3d transition metal dopants. Thus, we plot in Figure 4b the ratio of hydrogen solubility in M-ZrO_2 doped with a 3d transition metal to that in pure M-ZrO_2. These are essentially the same results in **Figure 3**b but with the x-axis recast as the dopants rather than μ_e.

The striking feature of our resulting plot is the emergence of a volcano-like dependence of hydrogen solubility across the 3d transition metals row. The peak is found at Co, which enhances the hydrogen solubility in M-ZrO_2 by more than 4 orders of magnitude at the given thermodynamic conditions. Moreover, we observe that Cr reduces hydrogen solubility to 1/4 its value in the undoped oxide, whereas Ti, V, and Mn have minor effects on the solubility at these conditions. The qualitative similarity and the intuitive underlying connection between the solubility volcano (**Figure 4**b) and the hydrogen pickup volcano (**Figure 4**a) are intriguing and encouraging, although the two curves do not have a one-to-one quantitative correspondence.

It is also important to clarify here that the effect of the alloying elements in Zr metal (whose nominal alloying fraction range between 1% and 5% in Figure 4 a) on hydrogen pickup is directly related to the effect of these very same elements on hydrogen solubility in ZrO_2 shown in Figure 4 b. The basis of the comparison between parts a and b of Figure 4 is that the effect of the alloying elements on hydrogen pickup is mainly through the dissolution of these elements in the ZrO_2 matrix. Our calculated Kröger-Vink diagrams detailed in section 6 of the Supplemental Material [17] indicate that in the oxygen rich part of M-ZrO_2 the solubility of transition metals range between 10^{-3} and 10^{-14} per ZrO_2 unit formula. The rationalization of this comparison is that these alloying elements have very limited solubility in Zr metal, and as such, they form dispersed intermetallic precipitates in Zr metal leaving behind a dissolved fraction significantly lower than

1-5% in Zr. As the oxidation front progresses, these intermetallic precipitates become part of the ZrO_2 oxide and they start to get oxidized themselves. However, these precipitates are dispersed and do not form a continuous percolated path in the host ZrO_2 to allow for an uninterrupted hydrogen transport. Both the intermetallic precipitates and the alloying elements that dissolved in the Zr metal provide the source terms for the alloying elements to dope ZrO_2 during oxidation. The starting total 1-5 % presence is sufficient to reach to the solubility limit of these alloying elements in ZrO_2. Consequently, the doped ZrO_2 oxide layer forms a continuous path through which hydrogen can dissolve and transport from the water interface all the way to the underlying Zr metal. Although the solubility of 3d transition metals in ZrO_2 is very small, their effect on the chemical potential of electrons and subsequently on hydrogen solubility is significant as Figure 4 b testifies. Here, we do not consider the changes in the microstructure of ZrO_2 due to different alloying elements. For example, Cr and Nb intermetallic precipitates would oxidize to Cr oxide and Nb oxide, respectively. Both oxides have different volumes and could lead to different stresses and strains in the surrounding ZrO_2 host, affecting the local reaction and transport kinetics for hydrogen. Similarly, we do not consider the kinetics of dissolving the alloying elements into ZrO_2. Section 13 of the Supplemental Material [17] elaborates more on: (1) the dissolution kinetics of precipitates into the ZrO_2 oxide layer, (2) the microstructural features of the oxide that are not considered here, and (3) the theoretical uncertainties in addressing the solubility of dopants in a metal oxide. We believe that these three factors are the main reasons of the qualitative discrepancies between the volcano of hydrogen pickup in Zr (Figure 4 a) and the volcano of hydrogen solubility in ZrO_2 (Figure 4 b).

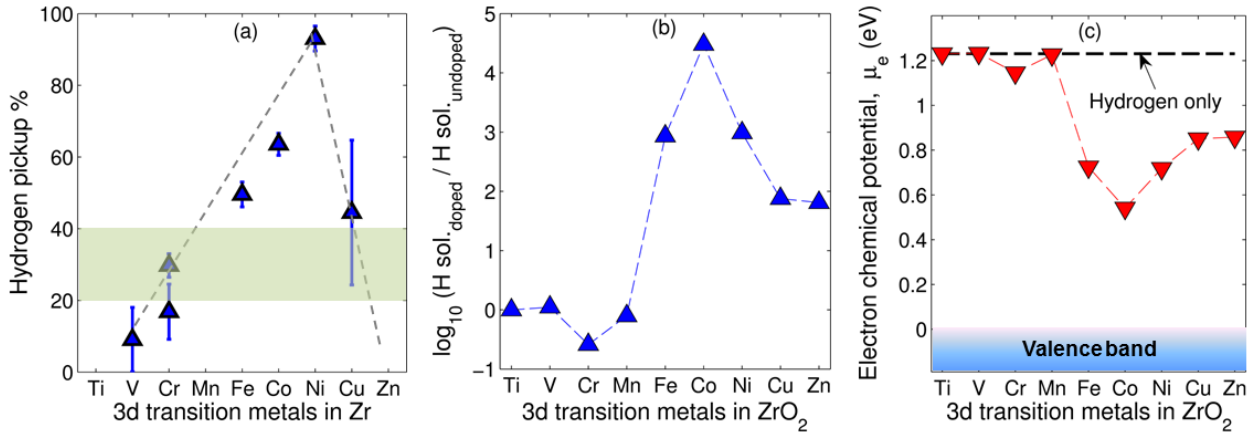

Figure 4. (a) Experimentally determined hydrogen pickup fraction in zirconium as a function of alloying across the 3d transition metal row. The data are based on zirconium alloys containing 1-5 % of a given transition metal and at temperatures between 573 K and 773 K. The shading indicates the hydrogen pickup fraction during the oxidation of pure zirconium metal. The figure is adapted from the data in ref. [14] (b) The ratio of hydrogen solubility in monoclinic ZrO_2 doped with 3d transition metals to that in the undoped oxide. The doping level for each metal is its equilibrium solubility in M-ZrO_2 under the thermodynamic conditions of interest. These solubilities range between 10^{-3} and 10^{-14} per ZrO_2 unit formula. (c) The chemical potential of electrons, μ_e, in monoclinic ZrO_2 co-doped with hydrogen and a transition metal. The horizontal dashed line indicates the value of the μ_e in the oxide doped with hydrogen only, without any transition metal. In (b) and (c), the data are evaluated at $T = 600$ K, $P_{O_2} = 1$ atm, and $P_{H_2O} = 1$ atm. The effect of varying T and P_{O_2} on the volcano shape in (b) is discussed in the Supplemental Material, Figure S28 [17].

To trace the origin of the volcano-shape of the predicted hydrogen solubility in **Figure 4**b, we plot in **Figure 4**c μ_e in M-ZrO_2 co-doped with hydrogen and a transition metal as a function of the dopants. We observe in **Figure 4**c that Ti, V, and Mn do not introduce any noticeable change in μ_e compared to the undoped M-ZrO_2 and hence they do not impact hydrogen solubility. On the other hand the rest of the 3d transition metals introduce noticeable p-type doping to an extent that depends on the dopant metal. The equilibrium μ_e in the case of Cr (1.15 eV in **Figure 4**c) is the closest to the intersection between the formation free energy lines of H_i and H_{Zr} which is at 1.19 eV in **Figure 3**c. This intersection is at the apex of the lowest

possible formation free energy (traced by the thick lines in **Figure 3**c) over all the hydrogen defects. Therefore, the solubility of hydrogen is minimal for Cr-doped M-ZrO_2 in **Figure 4**b. Any p-type doping that lowers μ_e below 1.19 eV increases hydrogen solubility by decreasing the formation free energy of H_i. Similarly, μ_e above 1.19 eV increases hydrogen solubility through the H_{Zr} defects. The p-type doping is maximal in cobalt-doped M-ZrO_2 where μ_e is pushed down to 0.54 eV as shown in **Figure 4**c. This explains the volcano shape around the peak of hydrogen solubility at Co in **Figure 4**b. The resulting behavior also supports the choice of μ_e as an optimal metric to discuss the effect of an alloying element on hydrogen solubility in M-ZrO_2 and the subsequent pickup in the underlying Zr metal. It is tempting to suggest the dominant oxidation of the alloying element in M-ZrO_2 instead of μ_e as the deciding factor for hydrogen solubility. However, this is not a better alternative. To explain our point, we extracted from the Kröger-Vink diagrams presented in section 6 of the Supplemental Material [17] the predominant oxidation state for the 3d transition metals raw in M-ZrO_2 at $T = 600$ K, $P_{O_2} = 1$ atm, and $P_{H_2O} = 1$ atm. These are: Sc^{3+}, Ti^{4+}, V^{5+}, Cr^{4+}, Mn^{4+}, Fe^{4+}, Co^{4+}, Ni^{4+}, Cu^{3+}, Zn^{2+}. If one considers the predominant oxidation state as the deciding factor for hydrogen solubility, one tends to conclude, for example, that all 4+ elements should lead to a hydrogen solubility comparable to that in pure undoped ZrO_2. The rational here is that 4+ elements are all neutral with respect to Zr^{4+}, and as such they would not induce any changes in μ_e. However, this is not the outcome because for each of these elements whose predominant oxidation state is 4+, there are also other oxidation states present and have lower concentration. Yet, the concentration of these minority defects is still high enough to affect the μ_e and subsequently impact the solubility

of hydrogen. So if one seeks a single metric that summarizes the complex defect equilibria of ZrO_2 co-doped with hydrogen and an alloying element, we recommend μ_e.

Finally, it was suggested recently based on DFT calculations that the volcano of hydrogen pickup in zirconium alloys shown in Figure 4a can be explained by the effect of the alloying element on the reaction energy of the recombination of H^+ and H^- at the grain boundaries of ZrO_2 [52]. This explanation starting from the reduced H^- species neither accounts for the availability and transport of electrons across the insulating ZrO_2 layer to reduce H^+ nor the solubility of H^+ in the oxide itself. Electron transport across ZrO_2 is thought to be the slowest process in Zr alloys corrosion [12], therefore it can decide the competition between hydrogen pickup and H_2 evolution. We discuss this point more in the next section.

E. Kinetic factors: proton reduction and hydrogen diffusion

Thus far we focused on the thermodynamic solubility of hydrogen as a function of μ_e that is established by the dopants in the oxide. μ_e also enters the kinetics of hydrogen pickup by impacting the ease of proton reduction at the surface of ZrO_2 and by dictating the predominant hydrogen defect; $H_i^{\bullet}$ v.s. $H_{Zr}^{'''}$. First we start by analyzing proton reduction. For a proton to be reduced, an electron has to *transport* from the metal/oxide interface to the oxide/water interface and then it has to *transfer* from the surface of the oxide to the adsorbed proton. We believe that bulk electron transport across ZrO_2 is the rate limiting step for proton reduction. This is tentatively corroborated by the cubic kinetics observed for the overall zirconium corrosion process [12], whose cathodic reaction is the proton reduction. Had the surface electron transfer been the rate limiting step in corrosion, linear kinetics of oxide growth with time should have been observed. Below we discuss how μ_e impacts electron transport and in section 15 of the

Supplemental Material [17] we show that changes in μ_e due to dilute doping does not affect the rate of electron transfer at equilibrium since the position of the conduction band edge at the surface of ZrO_2 is not affected by dilute doping [53,54]. Electron transport can proceed via electron or hole mechanism. However, the redox level H^+/H_2 of the proton reduction is closer to the conduction band of ZrO_2 at temperatures and pH of interest [55] (see Section 15 of the Supplemental Material [17]). Therefore, the only way for ZrO_2 to reduce H^+ and discharge H_2 gas from its surface is the transfer of electrons from its conduction band and not from its valence band. Thus, we focus the discussion below on electronic transport via the electron mechanism.

Electron transport is expected to be slowest in the oxygen rich part of the oxide [48,49], corresponding also to the oxide surface where the reduction of protons takes place. Electron transport is quantified by the electronic conductivity, σ, and in an insulator σ is proportional to the concentration of electrons in the conduction band, n_c. The latter is approximately exponentially dependent on μ_e by the relation $n_c \propto \exp(\frac{\mu_e - E_{CBM}}{k_B T})$ where E_{CBM} is the energy of the conduction band minimum. Consequently, p-type doping hinders the transport of electrons (via the electron mechanism) which are needed to reduce the adsorbed protons at the oxide/water interface. As a result, the residence time of the adsorbed protons at the surface of ZrO_2 increases, and the probability of their incorporation into the oxide increases. From a design point of view, it is desirable to introduce n-type conductivity or to minimize p-type doping in M-ZrO_2 in order to facilitate the transport of electrons to the protons at the surface. In **Figure 5**a, we plot $\log_{10}\left(\sigma(T,\mu_e)/\sigma^*(T)\right)$ as a function of μ_e at three temperatures, where $\sigma^*(T)$ is the electronic conductivity at μ_e that minimizes hydrogen solubility (at the dip of the valley in **Figure 3**a), and $\sigma(T,\mu_e)$ is the conductivity at any T and μ_e. For the sake of simplicity we assumed exponential

dependence of the conductivity on μ_e through n_c, and neglected any dopant-specific effect on the electron transport path [54]. At 600 K, a gain of 4 orders of magnitude in the electronic conductivity is achievable by maximizing μ_e. This maximum gain in conductivity with respect to $\sigma^*(T)$ decreases with increasing temperature.

This kinetic analysis suggests targeting an alloying element that can maximize μ_e in the oxygen rich part of M-ZrO_2 and accelerate proton reduction and H_2 evolution at the surface in order to minimize the entry of hydrogen through the oxide at a given time. This kinetic acceleration of proton reduction is anticipated to impede attaining the thermodynamic limit of the absorption of hydrogen into M-ZrO_2. In other words, ideally, the time to reach the thermodynamic equilibrium of hydrogen absorption can be increased beyond the time span of a corrosion cycle in the nuclear reactor (see Supplemental Material, section 16 [17]).

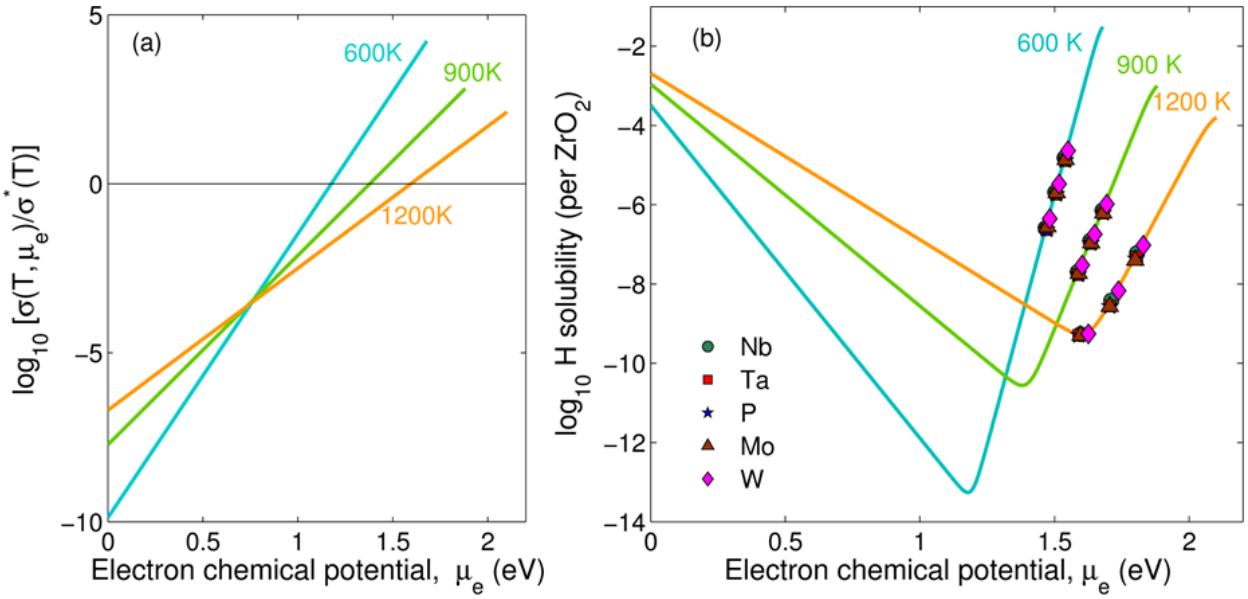

Figure 5. (a) The ratio of the electronic conductivity $\sigma(T,\mu_e)$ in M-ZrO_2 to $\sigma^*(T)$. $\sigma^*(T)$ is the electronic conductivity in the same oxide at the electron chemical potential, μ_e, that minimizes hydrogen solubility (the dip of the valley in Figure 3a for each temperature). (b) Mapping of 5 alloying elements on the hydrogen solubility curves that can maximize μ_e in ZrO_2.

On each isotherm the top data were evaluated at fixed doping concentration by the alloying element at 10^{-4} per ZrO_2 unit formula, the middle data at 10^{-5}, and finally the bottom data are at 10^{-6}. The calculations in (a) and (b) were performed assuming P_{O_2} = 1 atm, and P_{H_2O} = 1 atm which are representative of the oxygen rich part of ZrO_2 in contact with water.

Moreover, increasing μ_e changes the predominant hydrogen defect from $H_i^{\bullet}$ to $H_{Zr}^{\prime\prime\prime\prime}$ when μ_e exceeds its value that minimizes the hydrogen solubility. $H_{Zr}^{\prime\prime\prime\prime}$ has a binding energy of -2 eV and as such its diffusion barrier is higher than that of $H_i^{\bullet}$ by at least 2 eV. This is also a desirable effect since it reduces the flux of hydrogen diffusing through the oxygen rich part of the oxide. It is, however, also possible that $H_i^{\bullet}$ effective diffusion barrier is increased due to trapping by negatively charged defects such as substitutional defects of alloying elements with oxidation state less than 4+. A future investigation would be needed to assess whether the increase in $H_i^{\bullet}$ effective barrier can reach up to 2 eV, similar to the trapping effect imposed by the host zirconium vacancy on $H_{Zr}^{\prime\prime\prime\prime}$.

In order to accelerate hydrogen gas evolution, and reduce the hydrogen diffusion rate in ZrO_2, we then explore doping choices that can maximize μ_e by considering those elements that can exhibit oxidation states higher than that of Zr^{4+}. These elements are Nb, which is used in modern zirconium alloys, and Mo, P, Ta, and W which are new dopants that were not considered before. For these elements, we forced the concentration of dissolved dopants in ZrO_2 to 10^{-4}, 10^{-5}, and 10^{-6} per ZrO_2 unit formula. In **Figure 5b** we mapped these potential maximizers of μ_e on the hydrogen solubility curves. As expected when these elements dissolve up to 10^{-4} in ZrO_2 they increase the μ_e significantly. In fact W can achieve a larger μ_e because it can dissolve in the 6+ oxidation state in ZrO_2 (Supplemental Material section 6 [17]).

We note here that 10^{-4} is lower than the solubility limit of Ta and Nb in M-ZrO_2 whereas 10^{-6} is much higher than the solubility of Mo, P, and W (See section 6 of the Supplemental Material [17]). Thus, the desirable effect of Mo, P, and W on μ_e cannot be achieved by their thermodynamic tendency to dissolve in ZrO_2. However, the choice of these dopants is in the right direction of maximizing μ_e, and non-equilibrium material processing techniques [33], such as those involving irradiation [56], may enable the realization of the effect of these elements on the ZrO_2 electronic conductivity.

F. Design principles against hydrogen entry

Recommendations for the design of zirconium alloys with high resistance against hydrogen pickup can be extracted from the thermodynamic and kinetic analyses developed in the previous sections. To help in stating these recommendations, **Figure 6** compiles the main results of this work. The figure shows the calculated valley-shaped hydrogen solubility as a function of μ_e and T, and depicts the temperature-dependent loci of the minimum hydrogen solubility (triangles) and the maximum attainable μ_e (circles). These two sets of loci form the basis of the recommendations for designing zirconium alloys. In summary we recommend targeting a dopant that either thermodynamically minimizes the solubility of hydrogen in ZrO_2 (triangles), or maximizes μ_e, kinetically accelerates proton reduction and H_2 evolution at the surface, and promote the formation of the trapped $H_{Zr}^{'''}$ defect (circles). Here we discuss how we arrived at these recommendations by examining three doping regimes on the hydrogen solubility valley. These are marked on in Figure 6 as: (i) extreme p-type doping, (ii) doping that minimizes hydrogen solubility, and (iii) doping that maximizes μ_e.

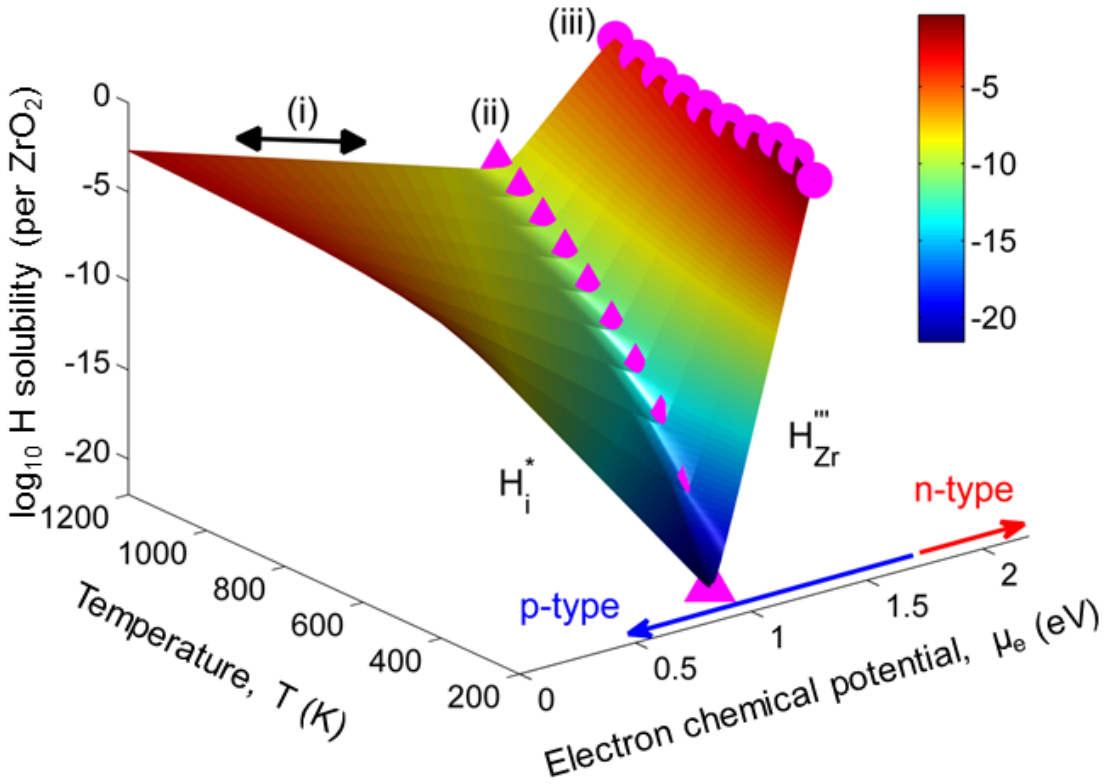

Figure 6. The calculated hydrogen solubility in monoclinic ZrO_2 as a function of electron chemical potential, μ_e, and temperature, T. The temperature-dependent loci of the minimum hydrogen solubility and maximum attainable μ_e are marked with triangles and circles, respectively. The two dominant hydrogen defects are also marked in the ranges of μ_e over which they predominate. The zones marked by (i), (ii), and (iii) represent the three different doping strategies which are discussed in the text. These calculations are performed assuming P_{O_2} = 1 atm, and P_{H_2O} = 1 atm, which are representative of the oxygen rich part of ZrO_2 in contact with water.

Our analysis shows that extreme p-type doping facilitates hydrogen pickup and so is undesirable. Such doping enhances the solubility of hydrogen in the oxide in the form of $H_i^{\bullet}$ as in zone (i), Figure 6. In addition, this doping significantly decreases the concentration of free electrons in the oxide. This, in turn, gives sufficient residence time for the adsorbed protons on the surface of ZrO_2 to be incorporated into the oxide before being reduced.

The origins of the undesirability of extreme p-type doping lead us to our first design recommendation; that is to reduce the hydrogen solubility in the oxide by alloying zirconium

with an element or a combination of elements such that, when these dissolve in M-ZrO_2, they establish a value for μ_e that minimizes hydrogen solubility. This is regime (ii), marked by the triangles in Figure 6, which span a wide range of temperatures applicable to the operation in the nuclear reactor and in accident conditions. At 600 K, normal operation temperature of light water cooled nuclear reactors, we find Cr to be an optimal element that minimizes hydrogen solubility as in **Figure 3**b. This finding is in line with the experimental observation that Cr additions can improve the resistance to hydrogen pickup [57]. The drawback of this approach is that proton reduction at the surface of M-ZrO_2 is hindered by virtue of the insufficient amount of electrons in the oxide, because all the triangle loci in Figure 6 lie in the p-type region of M-ZrO_2. Consequently, it is inevitable that some hydrogen will eventually reach the metal if this recommendation is adopted, but the advantage is that this amount is minimized.

Finally we consider alloying zirconium with elements which can maximize μ_e when dissolved in M-ZrO_2, and make it lie as close as possible to the loci marked by circles (regime iii) in Figure 6. We recommend such doping approach so that the reduction of adsorbed protons by electron transfer from the surface of ZrO_2 is fast by virtue of the enhancement of the electronic conductivity in the bulk of ZrO_2. In other words, the thermodynamic limit of dissolving substantial amount of hydrogen in M-ZrO_2 (in the form of $H_{Zr}^{'''}$) should be made very hard to attain by accelerating the proton reduction and H_2 gas evolution at the surface. Ideally, the time to reach equilibrium could be made significantly longer than the time span of a corrosion cycle in the nuclear reactor. While one can kinetically fight against hydrogen absorption, when μ_e is large it is likely that some hydrogen will still get into the oxide in the form of the $H_{Zr}^{'''}$ defect complex. Because this complex is strongly bound with a -2 eV binding

energy, it should have restricted mobility (with a migration barrier which is at least higher by 2 eV based on the binding energy of this defect, compared to a free interstitial proton). Thus, it is hard for this defect to diffuse and reach the underlying metal, another desirable factor that kinetically slows down the hydrogen pickup process at large μ_e conditions. In **Figure 5**b we showed that Nb, Ta, Mo, P, and W can maximize μ_e when they dissolve in M-ZrO_2. It is worth noting that although these elements are able to maximize μ_e, the actual value of μ_e is still far from the edge of the conduction band of ZrO_2 as shown in Figure 5b. Thus, in spite of the orders of magnitudes enhancement in the electronic conductivity achieved with these elements in comparison to 3d transition metals, the absolute magnitude of the conductivity remains low, compatible with the wide band gap and insulating character of ZrO_2. This absolute low conductivity is desirable to maintain slow corrosion of the zirconium alloy.

Our recommendation of doping ZrO_2 to maximize μ_e is supported by recent experiments which found improved resistance to hydrogen pickup in Zr-Nb alloys compared to Zr-3*d*-metal alloys [8]. Those authors suggested that this improvement is due to the ability of Nb to dissolve in ZrO_2 and subsequently increase the concentration of electrons in ZrO_2, but without a quantitative experimental or theoretical proof for this mechanism. In our work, we can unequivocally and quantitatively demonstrate that the improvement in the resistance to hydrogen pickup in Zr-Nb alloys is based on attaining a high μ_e in ZrO_2 when Nb dissolves into the oxide, and in turn, the easier reduction of adsorbed protons at the oxide surface followed by the discharge of H_2 gas from the surface. We also showed that Ta, Mo, P, W could be possible alternatives to Nb based on performance, availability and cost. More importantly we provided

physically justified design principles which can motivate further research for optimal compositions, for example by considering more than one dopant element at a time.

Lastly, the improvement of resistance to hydrogen pickup through ZrO_2 by Cr [57] (introducing p-type doping) and by Nb (introducing n-type doping) could not be reconciled prior to our work. The herein predictions of the solubility of hydrogen and the ability to reduce protons at the surface provides a unifying explanation for the way that both of these alloying elements can improve resistance of the ZrO_2 passive layer against hydrogen penetration.

IV. CONCLUSION

In this study, we wove ideas from catalysis and semiconductor defect physics to gain insights into the mechanism of hydrogen pickup in metal alloys. This problem is detrimental in many infrastructure and energy applications of alloys in corrosive conditions, including the nuclear energy industry. Enabled by our analysis of the charged defect equilibria in monoclinic ZrO_2, a passive oxide layer on Zr alloys, we identified the chemical potential of electrons μ_e as a physical metric that can control the absorption of hydrogen into ZrO_2. We showed that the calculated hydrogen solubility in ZrO_2 exhibits a valley-like dependence on μ_e.Thus, for designing zirconium alloys that are resistant against hydrogen-pickup, we suggest two strategies that rely on tuning μ_e by doping. We target either a dopant that thermodynamically minimizes the solubility of hydrogen in ZrO_2 (such as Cr) or a dopant that maximizes μ_e and kinetically accelerates H_2 evolution at the surface of ZrO_2 (such as Nb, Ta, W, P and Mo). Maximizing μ_e also enhances the predomination of the $H_{Zr}^{'''}$ defect, which is a trapped and less mobile form of hydrogen. Moreover, we showed that the computationally predicted dependence of hydrogen solubility in monoclinic ZrO_2 across the row of 3d transition metals exhibits a volcano-like

shape, similar to the earlier undecipherable experimental results for hydrogen pickup in zirconium across these metals.

This study provided the first physical and systematically quantified insights into how hydrogen absorption can depend on the composition of the native oxide film. The complexity of the microstructure [12] of the ZrO_2 passive layer during the corrosion process, radiation effects [56], and kinetic factors such as the dissolution rate of alloying elements in ZrO_2 and the diffusion of hydrogen in ZrO_2, warrant that future studies will add new components to this framework. Hydrogen embrittlement or hydrogen-induced crack-initiation is ubiquitous in many semiconducting [58,59] and metallic alloys including steels, Al- and Ni-based systems [60-64]. There is evidence that the severity of the embrittlement depends on the presence of a native oxide [15], through which hydrogen has to pass. However, there is a paucity of studying the role of the native oxides that grow on these alloys in regulating the entry of hydrogen. The approach and concepts developed in this work furnish the ground for similar studies of the oxides that grow on a broad range of structural metals that are susceptible to hydrogen embrittlement, such as steels and Ni-based alloys. Lastly, we believe that the computational approach presented here can also prove beneficial for the design of oxide fuel cell materials where hydrogen reactions and proton transport are important [65].

ACKNOWLEDGMENTS

We are grateful for the financial support from the Consortium for Advanced Simulation of Light Water Reactors (CASL), an Energy Innovation Hub for Modeling and Simulation of Nuclear Reactors under U.S. Department of Energy Contract No. DE-AC05-00OR22725, and for the computational support from National Science Foundation through the XSEDE Science Gateways program with the research allocation (TG-DMR120025). M. Yang is grateful for the MIT-China

Scholarship Council (CSC) Fellowship. We thank Ju Li for helpful discussions on charged defects in oxides, Harry L. Tuller for useful insights about electron transfer, Mujid Kazimi and Alex Mieloszyk for helpful input on the role of hydrogen in the nuclear regulatory framework, and Mujid Kazimi for a critical review of the manuscript.

Author contributions

B.Y. proposed the research. M.Youssef and B.Y. designed and performed the research, discussed the results, and wrote the manuscript. M.Youssef performed all the simulations except those for W, Ta, P, and Mo which were performed by M. Yang supervised by M. Youssef and B.Y.

REFERENCES

[1] C. G. Van de Walle, Hydrogen as a cause of doping in zinc oxide, Phys. Rev. Lett. **85**, 1012 (2000).
[2] A. Janotti and C. G. Van de Walle, Hydrogen multicentre bonds, Nat. Mater. **6**, 44 (2007).
[3] L. R. Merte *et al.*, Water-Mediated Proton Hopping on an Iron Oxide Surface, Science **336**, 889 (2012).
[4] R. Waser, Solubility of Hydrogen Defects in Doped and Undoped BaTiO3, J. Am. Ceram. Soc. **71**, 58 (1988).
[5] J. Chevalier, L. Gremillard, A. V. Virkar, and D. R. Clarke, The Tetragonal-Monoclinic Transformation in Zirconia: Lessons Learned and Future Trends, J. Am. Ceram. Soc. **92**, 1901 (2009).
[6] Y.-s. Kim, Y.-h. Jeong, and S.-b. Son, A study on the effects of dissolved hydrogen on zirconium alloys corrosion, J. Nucl. Mater. **444**, 349 (2014).
[7] H. C. Rogers, Hydrogen Embrittlement of Metals: Atomic hydrogen from a variety of sources reduces the ductility of many metals, Science **159**, 1057 (1968).
[8] A. Couet, A. T. Motta, and R. J. Comstock, Hydrogen pickup measurements in zirconium alloys: Relation to oxidation kinetics, J. Nucl. Mater. **451**, 1 (2014).
[9] M. Harada, R. Wakamatsu, M. Limback, B. Kammenzind, and S. W. Dean, The Effect of Hydrogen on the Transition Behavior of the Corrosion Rate of Zirconium Alloys, J. ASTM Int., 101117 (2008).
[10] A. Couet, A. T. Motta, B. d. Gabory, and Z. Cai, Microbeam X-Ray Absorption Near-Edge Spectroscopy study of the oxidation of Fe and Nb in zirconium alloy oxide layers, J. Nucl. Mater.
[11] S. T. Korhonen, M. Calatayud, and A. O. I. Krause, Stability of Hydroxylated (1̄11) and (1̄01) Surfaces of Monoclinic Zirconia:□ A Combined Study by DFT and Infrared Spectroscopy, J. Phys. Chem. C **112**, 6469 (2008).
[12] B. Cox, Some thoughts on the mechanisms of in-reactor corrosion of zirconium alloys, J. Nucl. Mater. **336**, 331 (2005).
[13] M. Youssef and B. Yildiz, Intrinsic point-defect equilibria in tetragonal ZrO_2: Density functional theory analysis with finite-temperature effects, Phys. Rev. B **86**, 144109 (2012).
[14] B. Cox, M. J. Davies, and A. D. Dent, The Oxidation and Corrosion of Zirconium and its Alloys, Part X. Hydrogen Absorption during Oxidation in Steam and Aqueous Solutions, 1960.

[15] B. P. Somerday, P. Sofronis, K. A. Nibur, C. San Marchi, and R. Kirchheim, Elucidating the variables affecting accelerated fatigue crack growth of steels in hydrogen gas with low oxygen concentrations, Acta Mater. **61**, 6153 (2013).
[16] M. Youssef and B. Yildiz, Hydrogen defects in tetragonal ZrO_2 studied using density functional theory, Phys. Chem. Chem. Phys. **16**, 1354 (2014).
[17] See Supplemental Material at [URL will be inserted by publisher] for Additional details and analyses about the defects considered in this study, uncertainty analysis for the valley and volcano of H solubility, discussion about the electron transfer from ZrO_2 surface, and discussion about the performance of standard DFT.
[18] R. F. W. Bader, A quantum theory of molecular structure and its applications, Chem. Rev. **91**, 893 (1991).
[19] W. Tang, E. Sanville, and G. Henkelman, A grid-based Bader analysis algorithm without lattice bias, J. Phys.: Condens. Matter **21**, 084204 (2009).
[20] D. Shrader, S. M. Khalil, T. Gerczak, T. R. Allen, A. J. Heim, I. Szlufarska, and D. Morgan, Ag diffusion in cubic silicon carbide, J. Nucl. Mater. **408**, 257 (2011).
[21] U. Otgonbaatar, W. Ma, M. Youssef, and B. Yildiz, Effect of Niobium on the Defect Chemistry and Oxidation Kinetics of Tetragonal ZrO_2, J. Phys. Chem. C **118**, 20122 (2014).
[22] D. W. McComb, Bonding and electronic structure in zirconia pseudopolymorphs investigated by electron energy-loss spectroscopy, Phys. Rev. B **54**, 7094 (1996).
[23] R. H. French, S. J. Glass, F. S. Ohuchi, Y. N. Xu, and W. Y. Ching, Experimental and theoretical determination of the electronic structure and optical properties of three phases of ZrO_2, Phys. Rev. B **49**, 5133 (1994).
[24] G. Makov and M. C. Payne, Periodic boundary conditions in *ab initio* calculations, Phys. Rev. B **51**, 4014 (1995).
[25] S. Baroni, S. de Gironcoli, A. Dal Corso, and P. Giannozzi, Phonons and related crystal properties from density-functional perturbation theory, Rev. Mod. Phys. **73**, 515 (2001).
[26] J. C. Garcia, L. M. R. Scolfaro, A. T. Lino, V. N. Freire, G. A. Farias, C. C. Silva, H. W. L. Alves, S. C. P. Rodrigues, and E. F. da Silva, Structural, electronic, and optical properties of ZrO2 from ab initio calculations, J. Appl. Phys. **100**, 104103 (2006).
[27] X. Zhao and D. Vanderbilt, Phonons and lattice dielectric properties of zirconia, Phys. Rev. B **65**, 075105 (2002).
[28] Y. Kumagai and F. Oba, Electrostatics-based finite-size corrections for first-principles point defect calculations, Phys. Rev. B **89**, 195205 (2014).
[29] C. W. M. Castleton, A. Höglund, and S. Mirbt, Managing the supercell approximation for charged defects in semiconductors: Finite-size scaling, charge correction factors, the band-gap problem, and the *ab initio* dielectric constant, Phys. Rev. B **73**, 035215 (2006).
[30] L. Wang, T. Maxisch, and G. Ceder, Oxidation energies of transition metal oxides within the GGA+U framework, Phys. Rev. B **73**, 195107 (2006).
[31] J. M. W. Chase, *NIST-JANAF Thermochemical Tables* (American Institute of Physics, Woodbury, N. Y., 1998).
[32] M. Todorova and J. Neugebauer, Extending the Concept of Defect Chemistry from Semiconductor Physics to Electrochemistry, Phys. Rev. Applied **1**, 014001 (2014).
[33] C. Suryanarayana, *Non-equilibrium processing of materials* (Elsevier, 1999), Vol. 2.
[34] G. Kresse and D. Joubert, From ultrasoft pseudopotentials to the projector augmented-wave method, Phys. Rev. B **59**, 1758 (1999).
[35] G. Kresse and J. Hafner, *Ab initio* molecular dynamics for liquid metals, Phys. Rev. B **47**, 558 (1993).

[36] G. Kresse and J. Hafner, *Ab initio* molecular-dynamics simulation of the liquid-metal–amorphous-semiconductor transition in germanium, Phys. Rev. B **49**, 14251 (1994).
[37] G. Kresse and J. Furthmüller, Efficiency of ab-initio total energy calculations for metals and semiconductors using a plane-wave basis set, Comput. Mater. Sci. **6**, 15 (1996).
[38] G. Kresse and J. Furthmüller, Efficient iterative schemes for *ab initio* total-energy calculations using a plane-wave basis set, Phys. Rev. B **54**, 11169 (1996).
[39] J. P. Perdew, K. Burke, and M. Ernzerhof, Generalized Gradient Approximation Made Simple, Phys. Rev. Lett. **77**, 3865 (1996).
[40] J. P. Perdew, K. Burke, and M. Ernzerhof, Generalized Gradient Approximation Made Simple [Phys. Rev. Lett. 77, 3865 (1996)], Phys. Rev. Lett. **78**, 1396 (1997).
[41] J. Heyd, G. E. Scuseria, and M. Ernzerhof, Hybrid functionals based on a screened Coulomb potential, J. Chem. Phys. **118**, 8207 (2003).
[42] A. V. Krukau, O. A. Vydrov, A. F. Izmaylov, and G. E. Scuseria, Influence of the exchange screening parameter on the performance of screened hybrid functionals, J. Chem. Phys. **125** (2006).
[43] R. Ramprasad, H. Zhu, P. Rinke, and M. Scheffler, New Perspective on Formation Energies and Energy Levels of Point Defects in Nonmetals, Phys. Rev. Lett. **108**, 066404 (2012).
[44] J. P. Perdew, A. Ruzsinszky, G. I. Csonka, O. A. Vydrov, G. E. Scuseria, V. N. Staroverov, and J. Tao, Exchange and correlation in open systems of fluctuating electron number, Phys. Rev. A **76**, 040501 (2007).
[45] P. Mori-Sánchez, A. J. Cohen, and W. Yang, Localization and Delocalization Errors in Density Functional Theory and Implications for Band-Gap Prediction, Phys. Rev. Lett. **100**, 146401 (2008).
[46] A. Togo, F. Oba, and I. Tanaka, First-principles calculations of the ferroelastic transition between rutile-type and $CaCl_2$-type SiO_2 at high pressures, Phys. Rev. B **78**, 134106 (2008).
[47] P. E. Blöchl, O. Jepsen, and O. K. Andersen, Improved tetrahedron method for Brillouin-zone integrations, Phys. Rev. B **49**, 16223 (1994).
[48] R. W. Vest, N. M. Tallan, and W. C. Tripp, Electrical Properties and Defect Structure of Zirconia: I, Monoclinic Phase, J. Am. Ceram. Soc. **47**, 635 (1964).
[49] A. Kumar, D. Rajdev, and D. L. Douglass, Effect of Oxide Defect Structure on the Electrical Properties of ZrO_2, J. Am. Ceram. Soc. **55**, 439 (1972).
[50] J. Xue, Nonstoichiometry and Point Defect Structure of Monoclinic and Tetragonal Zirconia □(□$ZrO_{2□+□δ}$□)□J. Electrochem. Soc. **138**, 36C (1991).
[51] K. Momma and F. Izumi, VESTA 3 for three-dimensional visualization of crystal, volumetric and morphology data, J. Appl. Crystallogr. **44**, 1272 (2011).
[52] M. Lindgren and I. Panas, Impact of additives on zirconium oxidation by water: mechanistic insights from first principles, R. Soc. Chem. Adv. **3**, 21613 (2013).
[53] S. R. Morrison, *Electrochemistry at Semiconductor and Oxidized Metal Electrodes* (Plenum Press, New York, 1984).
[54] R. Memming, *Semiconductor Electrochemistry* (WILEY-VCH, Weinheim, 2001).
[55] Y. Xu and M. A. A. Schoonen, The absolute energy positions of conduction and valence bands of selected semiconducting minerals, Am. Mineral. **85**, 543 (2000).
[56] G. S. Was, *Fundamentals of Radiation Materials Science* (Springer, Berlin, 2007).
[57] F. Garzarolli, R. Schumann, and E. Steinberg, in *Zirconium in the Nuclear Industry: Tenth International Symposium, ASTM STP 1245, Philadelphia, USA* (ASTM International, 1994), pp. 709.
[58] G. Moras, L. C. Ciacchi, C. Elsässer, P. Gumbsch, and A. De Vita, Atomically Smooth Stress-Corrosion Cleavage of a Hydrogen-Implanted Crystal, Phys. Rev. Lett. **105**, 075502 (2010).
[59] S. Ogata, F. Shimojo, R. K. Kalia, A. Nakano, and P. Vashishta, Environmental effects of H_2O on fracture initiation in silicon: A hybrid electronic-density-functional/molecular-dynamics study, J. Appl. Phys. **95**, 5316 (2004).

[60] J. Song and W. A. Curtin, Atomic mechanism and prediction of hydrogen embrittlement in iron, Nat. Mater. **12**, 145 (2013).
[61] M. Dadfarnia, P. Novak, D. C. Ahn, J. B. Liu, P. Sofronis, D. D. Johnson, and I. M. Robertson, Recent Advances in the Study of Structural Materials Compatibility with Hydrogen, Adv. Mater. **22**, 1128 (2010).
[62] D. F. Johnson and E. A. Carter, Hydrogen in tungsten: Absorption, diffusion, vacancy trapping, and decohesion, J. Mater. Res. **25**, 315 (2010).
[63] P. A. Burr, S. T. Murphy, S. C. Lumley, M. R. Wenman, and R. W. Grimes, Hydrogen solubility in zirconium intermetallic second phase particles, J. Nucl. Mater. **443**, 502 (2013).
[64] R. J. Zamora, A. K. Nair, R. G. Hennig, and D. H. Warner, *Ab initio* prediction of environmental embrittlement at a crack tip in aluminum, Phys. Rev. B **86**, 060101 (2012).
[65] L. Malavasi, C. A. J. Fisher, and M. S. Islam, Oxide-ion and proton conducting electrolyte materials for clean energy applications: structural and mechanistic features, Chem. Soc. Rev. **39**, 4370 (2010).